

---

# COMPARATIVE STUDY OF STATE-BASED NEURAL NETWORKS FOR VIRTUAL ANALOG AUDIO EFFECTS MODELING

---

A PREPRINT

**Riccardo Simionato**  
Department of Musicology  
University of Oslo  
Oslo, Norway  
riccardo.simionato@imv.uio.no

**Stefano Fasciani**  
Department of Musicology  
University of Oslo  
Oslo, Norway  
stefano.fasciani@imv.uio.no

## ABSTRACT

Analog electronic circuits are at the core of an important category of musical devices, which includes a broad range of sound synthesizers and audio effects. The nonlinear features of their passive and active electronic components give analog musical devices a distinctive timbre and sound quality, making them highly desirable. The development of software that simulates analog musical devices, known as virtual analog modeling, is a significant sub-field in audio signal processing. Artificial neural networks are a promising technique for virtual analog modeling. They have rapidly gained popularity for the emulation of analog audio effects, particularly recurrent networks. While neural approaches have been successful in accurately modeling distortion circuits, they require architectural improvements that account for parameter conditioning and low-latency response. Although hybrid solutions can offer advantages, black-box approaches can still be advantageous in some contexts. In this article, we explore the application of recent machine learning advancements for virtual analog modeling. In particular, we compare State-Space models and Linear Recurrent Units against the more common Long Short-Term Memory networks. These have shown promising ability in sequence-to-sequence modeling tasks, showing a notable improvement in signal history encoding. Our comparative study uses these black-box neural modeling techniques with a variety of audio effects. We evaluate the performance and limitations of these models using multiple metrics, providing insights for future research and development. Our metrics aim to assess the models' ability to accurately replicate energy envelopes and frequency contents, with a particular focus on transients in the audio signal. To incorporate control parameters into the models, we employ the Feature-wise Linear Modulation method. Long Short-Term Memory networks exhibit better accuracy in emulating distortions and equalizers, while the State-Space model, followed by Long Short-Term Memory networks when integrated in an encoder-decoder structure, and Linear Recurrent Unit outperforms others in emulating saturation and compression. When considering long time-variant characteristics, the State-Space model demonstrates the greatest capability to track history. The Long Short-Term Memory networks tend to introduce audio artifacts.

## 1 Introduction

The emulation of analog musical devices has become pervasive in digital products due to their distinct sound, appealing to producers and musicians. Analog circuits use components like operational amplifiers and diodes, whose nonlinear behaviors contribute to creating a unique sound. Replicating these devices, called Virtual Analog (VA) modeling, is now a crucial area in digital audio signal processing.

There are two possible approaches for emulating analog audio effects: physics-based and data-driven. Physics-based approaches discretize existing continuous-time models. Data-driven approaches identify a discrete model directly from discrete measurement data. Machine learning, as a data-driven method, has become widely used in audio modeling and is often integrated into more traditional digital signal-processing frameworks. Hybrid solutions, incorporating

knowledge of the modeling tasks, also exist and can offer advantages, but data-driven approaches can still be appealing in some contexts. While the former may not always be accurate enough, the latter may not be feasible for certain tasks.

Data-driven models, also called Black-box, being applicable to different audio modeling tasks, have already been proposed (Ramírez *et al.*, 2020a), but these usually involve large networks that are not suitable for low-latency and real-time applications. In addition, while machine learning modeling of nearly all types of analog effects has been investigated, they often do not provide a satisfactory response when continuously manipulating conditioning parameters, which is needed to offer users runtime control over the effect’s parameters.

This article presents a comparative study that applies recurrent and state-based neural network architectures to model audio effects with different complexities. Neural networks utilizing internal states and a recurrent formulation are often preferred among the different types of artificial neural networks. The most known type is the Recurrent Neural Networks (RNNs). A similar formulation is present in the State-Space Networks (SSMs). The internal states function as memory, making them particularly suitable in scenarios where time dependencies are crucial. Especially when the inputs are limited to one or a small segment of digital audio samples. For this reason, in this study, we consider Convolutional Neural Networks (CNNs) (LeCun *et al.*, 1998) only when integrated with RNNs (Simionato & Fasciani, 2022). The aim is to work with small input vectors while also considering long-term temporal dependencies. Therefore, we focus on state-based structures. Analog audio effects are dynamic physical systems that exhibit time-dependent characteristics: their output depends on previous internal states. Therefore, dynamic physical systems possess internal states that describe their physical evolution, similar to stateful machine learning algorithms.

We designed five architectures based on the popular Long Short-Term Memory (LSTM) (Hochreiter & Schmidhuber, 1997), the State-Space models (SSMs) (Gu *et al.*, 2022b; Gu & Dao, 2023), and the Linear Recurrent Unit (LRU) (Orvieto *et al.*, 2023). All models consider conditioning on control parameters using the Feature-wise Linear Modulation (FiLM) method (Perez *et al.*, 2018) and employ the Gated Linear Unit (GLU) (Dauphin *et al.*, 2017). The architectures have a limited computational complexity, measured in the number of floating points operations per output audio sample, ensuring theoretical real-time computational capabilities on consumer-grade devices. The designed architectures also present limited intrinsic input-output audio samples latency, which we have limited to a maximum of 64 samples (1.33 ms). Specifically, we refer to the intrinsic latency given by the architecture constraints, neglecting the latency given by the external DSP processing. This latency is due to the lag between the time index of the input and output samples.

Section 2 reviews the recent advancements in modeling analog devices, with a specific focus on the benefits and drawbacks of the recent deep learning methods against other data-driven methods. Section 3 details the methodology, architectures, losses, and datasets used in our experiments. Section 4 presents the obtained results and the consequent discussion on the limit and strength of the current methodology.

## 2 Background

Physics-based modeling for analog audio effects requires comprehensive knowledge of the circuit schematics and components. These circuits need to be mathematically modeled and solved. A numerical scheme is formulated, and the discrete equations are solved iteratively to generate the digital audio output.

Data-driven modeling is used when the inner circuitry of the audio effect is unknown. It treats the model as a mapping between input-output data: input-output measurements are used to approximate the system response. The procedure involves three main components: the dataset, candidate modeling techniques, and the validation process. The quality of the resulting model heavily depends on the selection of input signals, configuration of control parameters, and data collection. Data-driven approaches rely on measurements that are static representations of the system behavior, leading to greater difficulty in accurately emulating its dynamic aspects.

Common examples of data-driven approaches include the block-oriented Hammerstein model, the Wiener model, and their combinations (Schoukens & Tiels, 2017). In the Wiener model, a linear dynamic system is followed by a static nonlinearity, whereas in the Hammerstein model, the static nonlinearity precedes the linear dynamic system. These models offer a straightforward representation and are derived by estimating the model coefficients from real data using error-minimization techniques. A proposed method to classify whether a Wiener or a Hammerstein model should rather model the nonlinear system is in (Primavera *et al.*, 2018). Recent examples are for guitar distortion pedal (Eichas *et al.*, 2015) (Köper & Holters, 2020) (Darabundit *et al.*, 2019), amplifier (Jr & Bodmann, 2016) (Eichas *et al.*, 2017), distortion circuit (Eichas & Zölzer, 2016).

A more recent data-driven technique involves utilizing artificial neural networks (ANNs). ANNs consist of interconnected units called neurons, where each connection can transmit a signal. Each neuron processes these signals and can send them to other connected neurons. The transmitted signal is represented by a real number, and the neuron’s output

is determined by applying a nonlinear function to the sum of its weighted inputs. Training ANNs involve optimizing the network’s parameters to minimize the error between predicted and actual target values in a dataset. Gradient-based techniques, like backpropagation, are commonly used to optimize the network’s weights.

## 2.1 Neural Networks for Virtual Analog Modeling

In the last two decades, ANNs have been extensively used for modeling analog audio devices. In particular, traditional ML techniques, initially developed for different purposes, have been investigated to create models that emulate audio effects when taking and processing raw audio samples, such as traditional DSP techniques.

In an early attempt using machine learning for audio effect modeling (Mendoza, 2005), a multilayer feedforward network was utilized to learn a high-pass filter and the Ibanez Tube-Screamer distortion effect. The high-pass filter training led to unsatisfactory results, while the distortion effect demonstrated the ability of the network to learn distortion effects.

Other attempts used convolutional-based networks to model the preamplifier circuit from the Fender Bassman 56F-A vacuum-tube amplifier (Damskäg *et al.*, 2019a). The network consists of a stack of dilated causal convolution and fully connected layers. The dataset was simulated with different values of the gain, which is a variable resistor, and used to condition the model. The conditioning is realized in the convolutional layers and using the gated activation (Oord *et al.*, 2016). The work shows that CNNs accurately emulate the reference device better than a fully connected feedforward network and can respond to user control changes.

Using the same architecture, the Ibanez Tube Screamer, the Boss DS-1, and the Electro-Harmonix Big Muff Pi distortion pedals have been modeled as well (Damskäg *et al.*, 2019b). Here, the authors investigated more configurations, considering different dilation patterns and activation functions. In this work, the conditioning is not considered.

Similarly to a fully connected feedforward network, in which networks’ ability to track the past information depends on the amount of input received, the convolutional network performance depends on the receptive field; a longer receptive field requires a greater number of layers. To overcome this problem, Temporal Convolutional networks (TCN) have been proposed for optical dynamic range compressors such as Teletronix LA-2A Leveling Amplifier (Steinmetz *et al.*, 2022), which present longer time-variant characteristics than distortion units. TCNs’ strength consists of dilated convolutional networks with rapidly growing dilation factors ( $2^2$  and  $2^10$ ). Increasing the dilation factors increases, in turn, the receptive field and the ability of the networks when dealing with long dependencies while, in turn, not increasing the number of layers. The authors compared TCN networks with presenting receptive fields of 100, 300, and 1000 ms, respectively. The model with a receptive field of 300 ms provided the best performances. TCNs provide accurate and efficient implementation with respect to computational complexity. On the other hand, convolutional architectures present an intrinsic latency equal to the length of the receptive field, which is detrimental for live audio applications.

A model that combines different deep learning architectures was investigated in (Ramírez *et al.*, 2019). In this case, the model is divided into three parts: an adaptive front-end, latent space, and synthesis back-end. The front-end performs time-domain convolutions with the raw audio to map it into a latent space. The adaptive front-end consists of a convolutional encoder. The latent-space DNN modifies the latent representation of the input audio into a new latent representation, which is fed into the synthesis back-end. The synthesis back-end consists of an unpooling layer, a deep neural network with smooth adaptive activation functions (DNN-SAAF), and a single CNN layer. The SAAF (Hou *et al.*, 2017) is used as the nonlinearity for the last layer. Distortion, overdrive, and EQ effects have been modeled using this method.

In (Ramírez *et al.*, 2020a), the previously described architecture is further explored and compared with different variations and with the CNN architecture based on (Damskäg *et al.*, 2019a). The variations mainly consist of incorporating Bi-LSTMs or CNNs into the latent space. In this work, the target devices were Universal Audio Vacuum-Tube Preamplifier 610-B, Universal Audio Transistor-Based Limiter Amplifier 1176LN, and 145 Leslie Speaker Cabinet. The highest score in the listening test was obtained by the variation incorporating Bi-LSTM. Another variation based on Bi-LSTM and SAAF as latent-space modules is used for plate and spring reverberators (Ramírez *et al.*, 2020b). These architectures represent a general-purpose deep learning framework for modeling audio effects, which has been shown to be capable of accurately modeling different types of effects. On the other hand, the models are large networks with high computational complexity, leading to difficulty when considering efficient implementation. In addition, using the Bi-LSTM layer makes the architecture non-causal, not allowing real-time applications. This architecture also lacks conditioning possibility and focuses on modeling a static representation of the devices (i.e., fixed parameters).

The last group of machine-learning black-box modeling methods we review in this section are those based on RNNs. These have been applied to model a vacuum-tube amplifier (Covert & Livingston, 2013), where authors investigated different networks and input sizes in two scenarios: slightly distorted and overdriven signals. The networks’ input

included a variable number of audio samples. The network is autoregressive: it generates the output sample at the current time step using current and past input samples, but also output samples generated at previous time steps. The work presents preliminary experiments, and although the models resulted in poor performance, the work demonstrates the feasibility of modeling vacuum-tube amplifiers with RNNs.

RNNs, in particular LSTMs, have also been compared to CNNs when applied to the Ibanez Tube Screamer, the Boss DS-1, and the Electro-Harmonix Big Muff Pi distortion pedals (Wright *et al.*, 2019). The architecture consists of one RNN layer and one linear fully connected layer as an output layer with one unit. LSTM and GRU are compared as RNN layers varying the number of units. The input signal is extended to include an additional value representing the user control’s parameter. The results show that RNNs achieve similar accuracy to the CNN model while requiring significantly less computational cost and latency since requiring only the current input sample to predict the current output. LSTM performed better than GRU networks, and the error decreased when the number of units was increased.

Another RNN-based model utilized for the Klon Centaur guitar pedal circuit is presented in (Chowdhury, 2020), which is also compared with a WDF model of the same circuit. ML implementation resulted in better computational performance than the WDF model but sounded very similar, although the ML implementation slightly damped high frequencies. The architecture consists of a GRU layer and one linear fully connected layer with one unit as the output layer. Also, here, a single variable control parameter of the audio effect is added as an extra input to condition the inference of the networks.

A delay-based effect is investigated in (Mikkonen *et al.*, 2023), where a tape-based delay is modeled using GRU networks. Here, the delay trajectory is analyzed and extracted using impulse train signals. This trajectory is used to demodulate the signal before training the models or used to directly guide a delay-line built in a differentiable way and based on (Engel *et al.*, 2020) work.

RNNs rely on their internal memory mechanism to encode the history of the signal, but they can still suffer from remembering significant long-term dependencies. Indeed, LSTMs alone have not been successful for LFO delay-based effects, such as flanger and phaser. In (Wright & Välimäki, 2021), authors found it beneficial to use as extra input the LFO signal representing the frequency response of a time-varying system over time. The LFO signal is first extracted by analyzing the recording and then used to help the LSTM during the learning process. The extra input has shown to be beneficial to learning the LFO-based effect and can be freely controlled after model training, although in the study is considered only static parameter values and not LFO signal changing depth and width over time.

A sequence-to-sequence-based model, based on LSTMs, was designed and proposed for the case of another optical compressor, such as the TubeTech CL 1B compressor (Simionato & Fasciani, 2022), to help LSTMs’ memory. The network is based on two LSTM layers: one acts as an encoder, and the other acts as a decoder. The first takes a segment of past input samples together with the controls’ parameters, and the decoder takes the current input sample (in case of single output) or samples (in case of multi-sample output). The encoder, when processing the input, computes the internal states. These states are used as initial states for the second LSTM. These states represent a summary of the encoder input, which helps the decoder to infer the output. The sequence-to-sequence-based model is compared to LSTMs and fully connected networks, resulting in significantly better accuracy. The authors initially considered two control parameters, threshold, and ratio, while attack and release parameters were fixed. In (Simionato & Fasciani, 2023), the latter parameters were included. The model’s encoder was replaced with a convolutional layer, and the model was compared to TCNs. Sequence-to-sequence-based models allow for more responsiveness and interactivity but at the expense of an increasing computational cost.

Other works consider hybrid approaches. In (Parker *et al.*, 2019), fully connected neural networks exploit measurements within the circuits. Here, the network is embedded within a discrete-time state-space system and explored for diode-based guitar distortion circuits and the lowpass filter of the Korg MS-20 synthesizer. The method required measurements from the devices’ circuits, which are not always accessible. Continuing towards gray box approaches, (Kuznetsov *et al.*, 2020) is based on the Differentiable Digital Signal Processing (DDSP) framework and applies this concept to RC lowpass filter. Subsequently, the idea is applied to the parametric tone section of a guitar amplifier and a nonlinear guitar overdrive circuit in (Esqueda *et al.*, 2021). The technique learns the parameters of a circuit model from measurements of real devices using a Wiener-Hammerstein model consisting of two IIR filters and a feedforward artificial neural network. The IIR filters are, in this way, trainable and derived from the analysis of the circuit. This approach is also used in (Nercessian *et al.*, 2021). In this case, a cascade of biquad filters is trained, employing a Fourier transform, to model the BOSS MT-2 pedal distortion pedal. The model includes four tunable parameters. Differentiable Digital Filters have been applied for the case of a diode clipper circuit (Chowdhury & Clarke, 2022), showing higher accuracy and similar computation time when compared to traditional physics-based models. In (Wilczek *et al.*, 2022), the authors proposed to learn ordinary differential equations governing the first-order and the second-order diode clipper using fully connected layers and RNNs. The formulation similarly uses the discrete-time state-space as in (Parker *et al.*, 2019). Neural networks have also been investigated in the case of wave digital filter formulations (Darabundit *et al.*, 2022). A

tube amplifier circuit is simulated using multiport nonlinearities inside a wave digital filter and fully connected layers to learn features from a Kirchhoff-domain dataset. Similarly, in (Miklanek *et al.*, 2023), authors combine recurrent neural networks (RNNs) with the Kirchhoff nodal analysis to create a grey-box guitar amplifier model. Lastly, an example of gray box modeling in the case of the LA-2A leveling amplifier is (Wright & Välimäki, 2022), where it is modeled starting from the structure of a traditional digital compressor but using fully connected and RNN to predict the compressor’s parameters.

### 3 Methods

This study aims to identify which type of recurrent layer or architectural configuration accurately models different types of audio effects, if any. These insights can be used to understand the goodness and weakness of these models and determine which can better suit each audio effect. The states-based architectures offer advantages due to their ability to capture time dependencies in the data by utilizing internal states rather than solely relying on the input received at each iteration. In addition, we restrict the experimentation to relatively small networks fed by a small number of input segments, which present low computational complexity and low input-output latency, allowing implementation on real-time consumer-grade digital audio systems. The designed models are applied to different audio effects and finally evaluated using different metrics. To be noticed, the models presented here, having limited parameters, are not expected to lead to perfectly accurate emulation but a good starting point.

In the rest of this section, we first detail the four architectures used in this comparative study; then, we present the metrics we used for evaluating the trained models and the specific audio effects from which we collected the datasets. Finally, explain the process we used to train and test the models.

#### 3.1 Architectures

The following architectures, based on different types of recurrent layers, are compared in this study: **LSTM** (a), **ED** (b), **LRU** (c), and **S4D** (d). The four architectures are illustrated in Figure 1. **ED** is based on the concept of internal state sharing (Simionato & Fasciani, 2022). These architectures follow the same design, consisting of a linear, fully connected layer, a recurrent layer, and a conditioning block.

The number of input samples is identical for all architectures and set to 64. This choice represents a trade-off: on the one hand, there is the amount of past input information used to generate the current output, where more is typically better; on the other hand, there is the resulting input-output latency, which increases with the number of input samples. Our goal is to keep this latency below 1.33 ms (i.e., 64 samples at 48 kHz.). The input of all architectures is an array, including the 64 most recent input sample, used to generate the single current output sample. This implies that a new input sample enters the buffer with each inference cycle, while the oldest is discarded. Therefore, the set of the 64 most recent input samples constitutes the network input, which, after initial compression by the FC layer, is used to update the states in the recurrent layers. This approach aids the network in making predictions while maintaining a stateful design using truncated backpropagation through time. Predicting one sample at a time helps minimize the audible artifacts commonly associated with machine-learning models of audio effects, which arise from slight amplitude mismatches at the boundaries of consecutive output segments. Consequently, the model must perform predictions at an audio rate, one for each output audio sample. The models map a vector of 64 sample in one scalar output sample, give the internal states  $\mathbf{h}$ :

$$y_n = g(\mathbf{x}_n) = g(x_n, x_{n-1}, \dots, x_{n-62}, x_{n-63}; \mathbf{h}) \quad (1)$$

where  $n$  is the discrete time index, and  $g$  is the overall function describing the models. Before being fed into the recurrent layer (LSTM, LRU, S4D, or S6), the input samples array  $\mathbf{x}_n$  is processed by a fully connected layer that performs a linear projection:

$$\mathbf{u}_n = \mathbf{W}_l \mathbf{x}_n + \mathbf{b}_l \quad (2)$$

where  $\mathbf{u}_n$  is the linear projected vector having a size equal to the number of hidden units of the fully connected layer.  $\mathbf{W}_l$  and is the weights’ matrices, and  $\mathbf{b}_l$  the vector bias terms. The first two architectures use LSTMs as the recurrent layer, designed to improve the memory capacity of the vanilla RNN by incorporating internal mechanisms known as

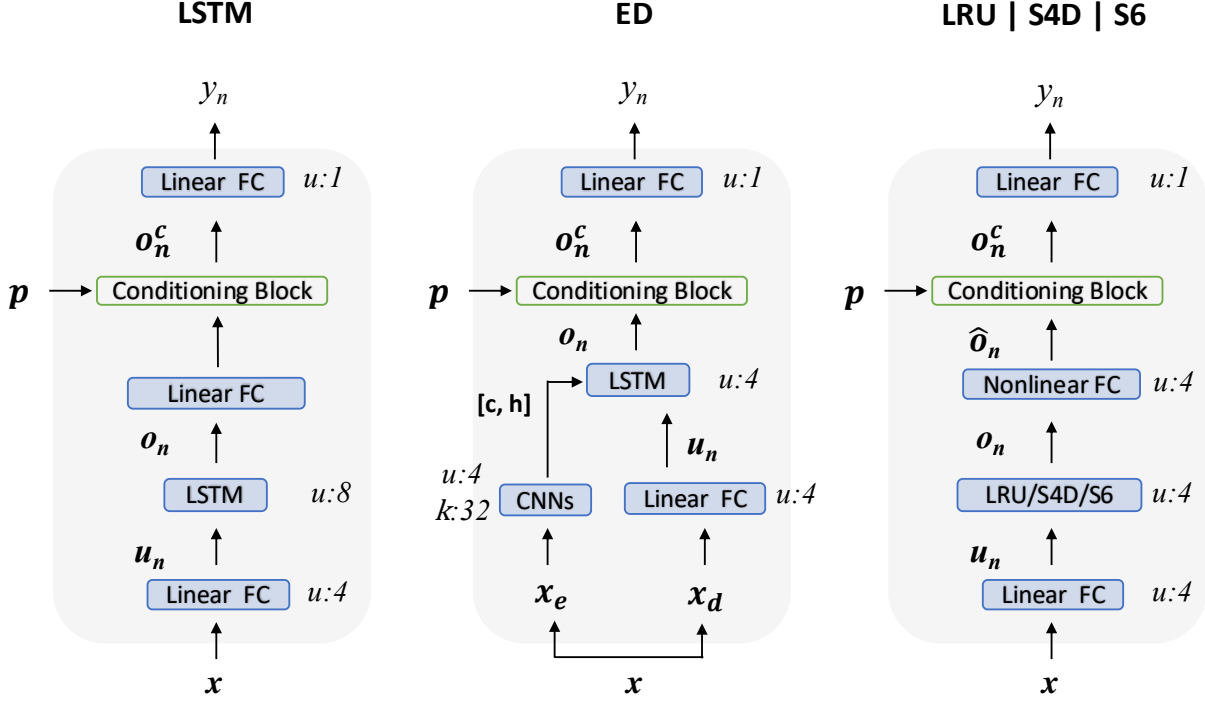


Figure 1: The four compared architectures: **LSTM**, **ED**, **LRU**, **S4D**, and **S6**. All architectures present the same structure: a fully connected layer, a recurrent layer, and a conditioning layer. For the case of **ED**, the input vector is equally split into two vectors,  $x_e$  and  $x_d$ .

gates, regulating the flow of information. The LSTM architecture is governed by the following equations:

$$\begin{aligned}
 f_n &= \gamma(W_f h_{n-1} + U_f u_n + b_f) \\
 i_n &= \gamma(W_i h_{n-1} + U_i u_n + b_i) \\
 o_n &= \gamma(W_o h_{n-1} + U_o u_n + b_o) \\
 c'_n &= \phi(W_c h_{n-1} + U_c u_n + b_c) \\
 c_n &= f_n \circ c_{n-1} + i_n \circ c'_n \\
 h_n &= o_n \circ \phi(c_n)
 \end{aligned} \tag{3}$$

where  $h_n$  is the hidden state vector,  $f$  is the forget gate,  $i$  the input gate, and  $o$  the output gate, and  $c$  is the cell state vector. The forget gate determines what information from previous steps should be kept or discarded. The input gate decides which information from the current step is relevant to add. The output gate determines the value of the next hidden state. Additionally, the cell state is updated by multiplying the forget vector and the input vector with new values that the neural network deems relevant. The forget vector and input vector are obtained using the sigmoid function, denoted by  $\gamma$ , which determines how much information should be kept. Values of 0 in this vector indicate information to be discarded, while a value of 1 indicates information to be kept. Furthermore, the  $\phi$  represents the hyperbolic tangent function, used to keep the value of the cell state between  $-1$  and  $1$ . Finally,  $W$  and  $U$  are the weights' matrices, and  $b$  the vector bias terms. After the LSTM layer, a linear FC layer reduces the dimensionality down to 4, ensuring consistency with all other models before proceeding to the conditioning block.

In the case of **ED**, the input split into two equal-size parts,  $x_d$  containing  $[x_n, \dots, x_{n-31}]$  and  $x_e$  containing containing  $[x_{n-32}, \dots, x_{n-63}]$ . The first part feeds two separate convolutional layers, which compute the states,  $[h, c]$ . These states are combined with the internal states of the LSTM layer computed during the previous iteration. A sigmoid function is applied to the LSTM internal states and then element-wise multiplied to  $[h, c]$ . This operation determines how much information should be taken from the computed  $[h, c]$ . The result of this operation represents the new LSTM's internal states. This process is detailed in Figure 2. The second part of the input vector is linearly transformed and fed into the second LSTM, following the same procedure as the other models.

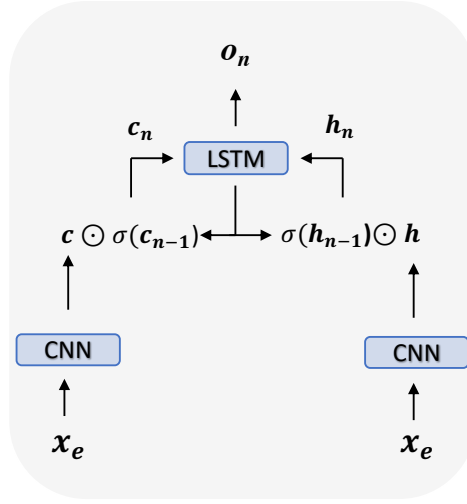


Figure 2: The states sharing process in **ED**: the encoder input  $x_e$  is passed to two convolutional layers, which produce the states  $[h, c]$ . These states are combined with  $[h_{n-1}, c_{n-1}]$ , which are the LSTM states of the previous iteration. The sigmoid function is applied to  $[h_{n-1}, c_{n-1}]$  and the results are element-wise multiplied to  $[h, c]$ . The outcome will be the new states for the LSTM layer  $[h_n, c_n]$ .

The third architecture is based on LRU. Compared to a vanilla RNN, the LRU uses a linear activation function to compute the hidden state instead of a nonlinear function. This modification allows the memory capability to improve significantly. The LRU equations are the following:

$$\begin{aligned} h_n &= W_h h_{n-1} + U_h u_n + b_h \\ o_n &= W_o h_n + b_o \end{aligned} \quad (4)$$

where  $h_n$  is the hidden state at time  $n$  and acts as 'memory' of the network,  $o_n$  the output vector. LRU keeps the recurrent layer linear but moves the nonlinearity to a subsequent fully connected layer. Additionally, to further enhance stability, the LRU incorporates a complex-valued diagonal recurrent matrix initialization and an exponential parameterization. At the same time, a normalization scheme for the hidden states is used to boost the efficiency and accuracy (Orvieto *et al.*, 2023).

Lastly, the SSMs operate by considering a continuous-time representation of the state-space formulation that is discretized to obtain the following equations:

$$\begin{aligned} h_n &= \bar{W}_A h_{n-1} + \bar{W}_B u_n \\ o_n &= \bar{W}_C h_n + \bar{W}_D u_n. \end{aligned} \quad (5)$$

In our study, we employ the diagonal state space model variant S4D (Gu *et al.*, 2022a), and newer S6 variant (Gu & Dao, 2023).

The remarkable ability of S4D to capture long-range dependencies stems from their utilization of a specific state matrix  $\bar{W}_A$  known as the "HiPPO matrix" (Gu *et al.*, 2020). This matrix is designed to encode all the past input history in  $h_n$ , finding a map from  $u_n$  to a higher dimensional space  $h_n$  that represents the compression of the history. The matrix allows the model to be conceptualized as a convolutional model that decomposes an input signal onto an orthogonal system of smooth basis functions. In this way, the state  $h_n$  encodes the history of the signal. In the diagonal form, the S4D model is defined by parameterizing its state matrix as a diagonal matrix, boosting the model's efficiency. By doing so, the basis kernels have closed-form formulas represented by normalized Legendre polynomials  $L_n(t)$ , resulting in the SSM decomposing the input signal  $u_n$  onto an infinitely long set of basis functions that are orthogonal with respect to an exponentially decaying measure.

In contrast, the S6 layer introduces input-dependent matrices. Specifically,  $\bar{W}_B$  and  $\bar{W}_C$  become dependent on the input and computed using a linear FC layer, while  $\bar{W}_A$  and  $\bar{W}_D$ 's parameters are independent of the input and learned during the training process.

The recurrent layer's output size will equal the number of hidden units of the layer. In the case of LRU and S4D, a fully connected layer with a hyperbolic tangent activation function also follows the recurrent layer to compensate for a lack

of nonlinear activation functions in these layers:

$$\hat{o}_n = \tanh(\mathbf{W}_{nl} \mathbf{o}_n + \mathbf{b}_{nl}) \quad (6)$$

The conditioning block is then applied just before the output layer, which consists of a linear fully connected layer with one unit, which is described in the following subsection. Placing the conditioning block after the recurrent layers rather than before has been found beneficial (Fasciani *et al.*, 2024a). This suggests that it is more beneficial for the networks to use the information given by the control parameters to project the output of the recurrent layer and determine the extent to which this information influences the final output rather than influencing the inference of the recurrent layer based on the control parameters.

Finally, the output layer, which is a fully connected layer with one unit, computes  $y_n$ :

$$y_n = (\mathbf{W}_{out} \mathbf{o}_n^c + b_{out}) \quad (7)$$

where  $\mathbf{o}_n^c$  is the output of the conditioning block, as detailed in Figure 3. Since the output layer has one unit,  $\mathbf{W}_{out}$  is a vector of the same dimensionality as  $\mathbf{o}_n^c$ .

The number of units is chosen to have approximately 800 trainable parameters among the architectures and effects since an identical number is achievable due to major differences in the layers. As a result, the selected **LSTM** and **ED** present 8 units in the recurrent layer and 4 in fully connected ones. **LRU** and **S4D** present 12 units in the recurrent layer, and 6 in fully connected ones. The number of trainable parameters also depends on the dimensional of the conditioning input  $p$ , equal to the number of variable parameters in the datasets.

### 3.1.1 Conditioning Block

The conditioning block consists of the FiLM method and the GLU layer, as in (Fasciani *et al.*, 2024a), and is illustrated in Figure 3. FiLM is a technique that applies an affine transformation to a vector based on conditioning values. The

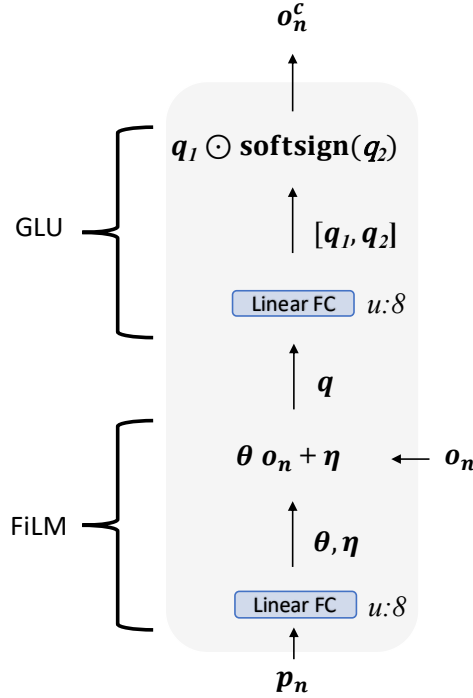


Figure 3: Conditioning block based on the FiLM method and the GLU layer. The GLU layer features the softsign activation,  $p$  denotes the conditioning vector, and  $\mathbf{o}_n$  represents the network’s internal representation of the input.

parameters vector  $p$ , if applicable, is the input to a linear fully connected layer. The output of this layer is then split into two vectors of equal size:  $\theta$  and  $\eta$ . If  $\mathbf{o}_n$  is the vector to which the transformation is to be applied, the output of the linear fully connected layer will have a length double of  $\mathbf{o}_n$ . Consequently, FiLM performs an affine transform on  $\mathbf{o}_n$  using  $\theta$  and  $\eta$ .



Following the projection, it is common to apply a function, such as ReLU or sigmoid, to determine the amount of information that should be passed. In our approach, we replace the activation function with a GLU layer. This layer is more stable than ReLU and exhibits faster learning compared to sigmoid. Similarly to the previous step, the GLU layer consists of a linear fully connected layer that takes the FiLM output vector as input and computes a vector with twice its length. The resulting output is then split equally into two vectors:  $\mathbf{q}_1$  and  $\mathbf{q}_2$ . A function is applied to  $\mathbf{q}_2$ , and the resulting output is multiplied element-wise with  $\mathbf{q}_1$ . Hence, the conditioning block is described by the following:

$$\begin{aligned} \mathbf{o}_n^c &= \mathbf{q}_1 \odot \text{softsign}(\mathbf{q}_2), \text{ with } \mathbf{q}_1 = \dot{\mathbf{o}}_n \mathbf{K}_1 + \mathbf{d}_1 \\ &\quad \mathbf{q}_2 = \dot{\mathbf{o}}_n \mathbf{K}_2 + \mathbf{d}_2 \\ &\quad \dot{\mathbf{o}}_n = (\boldsymbol{\theta} \mathbf{o}_n + \boldsymbol{\eta}). \end{aligned} \quad (8)$$

The GLU layer determines the flow of information through the network, acting as a logical gate. Typically, a sigmoid activation function is used for this purpose. However, in our approach, we introduce a softsign function instead. The softsign function controls the extent to which the control parameters should positively or negatively influence the final output. A value of 0 indicates a bypass, meaning no influence on the output. This allows for more flexibility.

Lastly, the presented models are designed to have limited computational complexity for the inference process. Specifically, we set the limit to 1.500 FLOPs per sample or 72 MFLOPs per second at 48 KHz. By doing so, the models feature  $\sim 750$  internal parameters. Table 1 reports the FLOPs per sample for each model.

Table 1: FLOPs per sample for each model considered in this study.

Model	Recurrent Layer	Conditioning Block	Total
LSTM	1040	120	1160
ED	928	120	1048
LRU	692	120	812
S4D	792	120	912
S6	864	120	984

### 3.2 Losses and Metrics

The models in this study take raw audio samples as input and produce raw audio samples as output. The most common losses used in this case include the Mean Squared Error (MSE), the Mean Absolute Error (MAE), and the Error-to-Signal Ratio (ESR). Based on our knowledge and supported by empirical experiments, there is no evidence suggesting that more complex loss functions could benefit the learning process, especially when modeling the transformation applied to a signal by a generic audio effect. While using specific and different loss functions for different effects may potentially yield better results, we decided to carry out this study using a fixed loss function across architectures and audio effects. This allows for a fair comparison between the trained models, as they all attempt to minimize the same loss function. Therefore, we selected the MSE for this comparative study as it helps to capture the dynamic aspects of the output signal more effectively (Simionato & Fasciani, 2023).

In addition, our quantitative evaluation is based on various metrics to assess the models from different perspectives. In the following expressions,  $y_n$  and  $\hat{y}_n$  represent the target and predicted signal and the symbol  $N$  represents the overall number of samples in the output signal.

The first metric is the root-mean-square energy (RMSE) error. RMSE error provides insights into the energy deviation between the target and prediction. The losses and metrics presented so far calculate the average difference between the target and prediction, which may hide large errors that occur only during signal transients. Transients, such as sharp attacks or decays, may represent a small fraction of the overall duration of an audio signal. In this case, we may obtain a relatively low error even with all transients poorly modeled. Therefore, we have included a metric related to the spectral flux, which considers the differences between pairs of spectrums computed on consecutive overlapping windows, as used in the library <sup>1</sup> developed after (Engel *et al.*, 2020):

$$\begin{aligned} M_{SF} &= \left| \left| \left( \left| |STFT(y_n)| - |STFT(y_{n-1})| \right| \right) \right. \right. \\ &\quad \left. \left. - \left( \left| |STFT(\hat{y}_n)| - |STFT(\hat{y}_{n-1})| \right| \right) \right| \right|_1 \end{aligned} \quad (9)$$

where the Short-Time Fourier Transform (STFT) is computed with a window size equal to 2048 and hop size equal to 512 samples. This metric emphasizes the ability to predict portions of the output sound with rapid changes.

<sup>1</sup><https://github.com/magenta/ddsp>

To account for the frequency response, we use the multi-resolution STFT (Engel *et al.*, 2020):

$$M_{STFT} = \frac{1}{N} \sum_m \left( \left| |STFT_m(y_n)| - |STFT_m(\hat{y}_n)| \right| \right)_1 + \frac{1}{N} \sum_m \left( \left| \log(|STFT_m(y_n)|) - \log(|STFT_m(\hat{y}_n)|) \right| \right)_1 \quad (10)$$

which compares linear and logarithmic spectral distances with varying frequency resolutions using the L1 norm. The error is calculated as the sum of the absolute values of the vectors. This metric quantifies the error between the spectra employing different resolutions. We compute the metrics using  $m = [256, 512, 1024]$  as resolutions.

Similarly, we compare the MFCCs to compute a metric linked to human sound perception:

$$M_{MFCC} = \frac{1}{N} \left( \left| |MFCC(y_n)| - |MFCC(\hat{y}_n)| \right| \right)_1 \quad (11)$$

where 1024 is the FFT length, and we have 80 Mel bands between 30 Hz and Nyquist frequency.

### 3.3 Audio Effects and Datasets

In this section, we introduce the audio effects selected for the study and the composition of their datasets. We proceeded to record the dataset using effects that were at our disposal. In particular, we selected the following effects: overdrive, saturation, equalization, low-pass filter, and compression. Table 2 summarizes all the datasets included in the study. Delay-based effects require a different approach than a direct black box (Wright & Välimäki, 2021), (Mikkonen *et al.*, 2023). For this reason, they are not included in this study.

The dataset we use is derived from the following hardware devices: Behringer OD300 overdrive pedal <sup>2</sup>, Behringer Neutron <sup>3</sup>'s overdrive module, Behringer Neutron's filter module in low-pass mode, TC Electronic Bucket Brigade Analog Delay used as a saturator <sup>4</sup>, CL 1B TubeTech <sup>5</sup> and Teletronix LA-2A <sup>6</sup> optical compressors. We have also collected data from two software VA plugins using (Fasciani *et al.*, 2024b): the Helper Saturator <sup>7</sup> and Universal Audio Pultec EQ <sup>8</sup>, because the hardware saturator presents no variable control parameter, and because we have no analog equalizer in our immediate availability.

**Overdrive** Both the overdrive devices feature the following control parameters: volume, distortion level, and tone. The OD300 is a distortion pedal that features two different types of distortion, labeled overdrive and distortion modes. To record the dataset, the unit was set to overdrive mode. The device was sampled at 5 different and equally spaced values for the distortion and tone knobs. Neutron's overdrive is a module integrated into the Neutron synthesizer. Thanks to the semi-modular nature of this device, we were able to isolate the overdrive module. We recorded the dataset's varying distortion and tone as we did for the OD300, but sampling 10 equally spaced values for each parameter. In both devices, the volume level controls an attenuator, and we fixed this parameter to the maximum (i.e., no attenuation).

**Filter** Similarly to the overdrive, the Behringer Neutron integrates a filter module, which features frequency cutoff and resonance knobs. The filter can be set as low-pass, high-pass, and band-pass. We isolated the module and recorded the dataset at 10 equally spaced values for the cutoff and 5 for the resonance, selecting the low-pass filter type. The filter was disconnected from the ADSR envelope module.

**Saturator** Helper Saturator software emulates analog saturation, in particular tube and tape saturation. The software presents four parameters: lowpass and highpass cutoffs, saturation type switch (tape or tube), and saturation level. We recorded the dataset for 10 different values of the saturation level. The saturation switch was set to tape mode. Lowpass and highpass cutoffs were set to 20 and 20000 Hz, respectively.

<sup>2</sup><https://www.behringer.com/product.html?modelCode=P0608>

<sup>3</sup><https://www.behringer.com/product.html?modelCode=POCM5>

<sup>4</sup><https://www.tcelectronic.com/product.html?modelCode=P0EBV>

<sup>5</sup><http://www.tube-tech.com/cl-1b-opto-compressor/>

<sup>6</sup><https://www.uaudio.com/hardware/la-2a.html>

<sup>7</sup><https://www.waproductio.com/plugins/view/helper-saturator>

<sup>8</sup><https://www.uaudio.com/uad-plugins/equalizers/pultec-passive-eq-collection.html>

**Equalizer** The software plug-in Universal Audio Pultec Passive Equalizer emulates the tube-based equalizer Pultec EQP-1A. The effect presents low-frequency ([20, 30, 60, 100] Hz) and high-frequency ([3, 4, 5, 8, 10, 12, 16]kHz) switches to select the frequencies to boost or cut using the respective boost and attenuator knobs ([0,10]). Additionally, the emulation also has a bandwidth knob ([0,10]). The equalizer boosts and cuts the selected frequency bands, giving some saturation simultaneously. In this case, we recorded the dataset varying the boost and attenuator knobs at 5 different equally-spaced values up to half of their range, setting 60 Hz as the low-frequency switch value and 0 (sharp) as the bandwidth.

**Compressor/Limiter** The CL 1B and the LA-2A are analog optical compressors. In optical compressors, a lighting-emitting element is fed with the audio signal that illuminates a light-sensitive resistor. The input signal’s amplitude determines the element’s brightness, which, in turn, changes the resistance in the gain attenuation circuit. We recorded the dataset directly from the compressor. The CL 1B compressor dataset presents four parameters: attack, release, ratio, and threshold. We consider three equally spaced values for the ratio, attack, and release time and four values for the threshold. On the other hand, LA-2A presents the peak reduction knob indicating the amount of compression ([0,100]) and a mode switch (limiter, compression). We consider 10 equally spaced values for the peak reduction.

Table 2: Datasets with related parameters and ranges considered in the study.

	Type	Parameters	Range	Combinations
OD300 <sup>1</sup>	Overdrive	Level Tone	[min, max] [min, max]	25
Neutron Overdrive module <sup>1</sup>	Overdrive	Level Tone	[min, max] [min, max]	100
Neutron Filter module <sup>1</sup>	Low pass filter	Cutoff Resonance	[min, max] [min, max]	100
Helper Saturator <sup>2</sup>	Saturator	Saturation Saturation Type	[min, max] Tape	10
Pultec Passive EQ <sup>2</sup>	Equalizer	Low frequency Frequency booster Bandwidth Frequency Attenuator	60 Hz [0,10] 0 [0,10]	25
LA-2A <sup>1 3</sup>	Optical Compressor	Peak Reduction Switch Mode	[0,100] [Compressor,Limiter]	20
CL 1B <sup>1</sup>	Optical Compressor	Threshold Ratio Attack Release	[-40, 0] dB 1:[1, 10] [5, 300] ms [0.005, 10] s	108

### 3.3.1 Data Collection

The data collection process was carried out using a MOTU M4 audio interface to feed a selection of audio signals into the system and simultaneously record its output. To achieve this, the left input channel of the audio interface was connected to the left output channel of the interface itself. The right input channel of the audio interface was connected to the output of the device, and the input of the device to the right output channel of the audio interface. This allows effective recording of both the device’s input and output signals, compensating for the minor sound coloring and latency of the audio interface. The audio data was recorded at a sampling rate of 48 kHz.

The input mono signal has a duration of 45 seconds for each parameter combination and includes a variety of sounds, such as frequency sweeps covering a range of 20 Hz to 20 kHz, white noises with increasing amplitudes (both linear and logarithmic), recordings of instruments such as guitar, bass, drums (both loops and single notes), vocals, piano, pad sounds, and sections from various electronic and rock songs. Finally, the control parameter of each effect was mapped to the range of [0,1].

### 3.4 Experimenting and Learning

The models are trained for 200 epochs and using the Adam (Kingma & Ba, 2014) optimizer with a gradient norm scaling of 1 (Pascanu *et al.*, 2013). The training was stopped earlier in case of no reduction of validation loss for 10 epochs. We design a learning rate with an exponential decay according to the formula:  $lr = LR * 0.25^e$ , where LR is the initial learning rate and it is set to  $3 \cdot 10^{-4}$ , and  $e$  is the number of the epochs. Test losses and evaluation metrics are computed using the model’s weights that minimize the validation loss throughout the training epochs. Finally, the input signal is split into segments of 2400 samples (equivalent to 50 ms) to be processed before updating the weights. Considering the network architecture described in Section 3.1, in which a buffer of the 64 most recent samples is used as input, training layers with states necessitates sequential input-output examples. Consequently, our implementation adopts an input shape of  $(B, L, F)$ , which is set to  $(B, 1, 64)$ , where  $B$  denotes the arbitrary batch size,  $L$  the sequence length, and  $F$  the input dimensionality, often identified as the number of input features. This configuration considers the 64 input samples as the vector of input features at the current sampling instant.

We adopted the same learning schedule and minibatch size for all models across all datasets. As explained in Section 3.3, we collected the datasets using the same approach and the same input file to minimize the difference among them. However, it is important to highlight that each dataset and modeling task may benefit from specific adjustments to achieve more accurate results. Different datasets and tasks may require slightly different learning rate schedules; an excessively slow or fast learning rate can lead to suboptimal solutions. The number of samples to process before updating the weights referred to as the minibatch size, impacts the frequency of updating weights: larger sizes may result in faster convergence but poorer generalization, while smaller sizes can aid generalization but may require additional epochs.

The composition of the training, validation, and test sets is identical across datasets. We used 80% for the training set, 10% for the validation set, and the remaining 10% for the test set. For effects with variable control parameters, each 45s recording in the dataset is associated with a specific combination of the effect parameters. The 80 – 10 – 10% split was carried out at the individual recording level, ensuring that all control parameter combinations present an equal share in each subset and are equally used for training and evaluation of the model. The initial 10% of all the recordings are used as the test set. The following 10% portion of the recordings is used as a validation set, while the remaining parts were used as the training set. Minor manual adjustments are made to ensure that splitting points fall within segments of silence.

## 4 Results

The evaluation is based on the metrics described in Section 3.2 and presented in Table 4. The MSE loss and the epoch-related epoch resulting in lower validation loss during training are reported in Table 3. The losses and the metrics consider all conditioning scenarios and provide an average error across all combinations of parameters. To further verify the model’s capacity to learn the conditioned effect, we provide a series of plots that compare the target signal with the predictions generated by the four distinct architectures. For these plots, we chose the modeling scenario that we believe to be the most challenging based on the effect parameters used as conditioning factors for the networks. Except for the low-pass filter, this typically involves parameters at the maximum of the selected range since the output signal, under these conditions, is likely to deviate most significantly from the input. Regarding the low-pass filter, the parameters are configured for minimum cutoff and maximum resonance. The plots show the RMSE in Figure 4, and the spectrograms in Figure 5. For datasets including conditioning parameters, the plots showing predictions versus the target are generated for a 2.5 seconds input signal containing bass, guitar, and drum loop sound. These input signals are part of the respective test sets. To ensure a clearer comparative visualization of the spectral flux, we use only the first 1.25 seconds.

In the OD300 and Neutron’s overdrive dataset, the **LSTM** model presents the lowest MSE and ESR, indicating better general amplitude matching between target and prediction. On the other hand, the **S4D** and **S6** present better accuracy when considering the transients, the RMS envelope, and frequency-related content. This can be observed from the general lower error in terms of RMSE, spectral flux, STFT, and MFCC. In the case of maximum distortion, we can notice **LRU** prediction having significantly lower energy than other models. Notably, the spectrograms shown in Figure 5 illustrate that **S4D** and **S6** models better match the energy in the harmonics at higher frequency regions. **LRU** fails to generate the harmonics in the OD300 case while **ED** presents the opposite behavior in Neutron’s overdrive. Models trained on the Neutron OD dataset exhibit larger errors, suggesting that this dataset presents a more challenging modeling case for the investigated architectures. This challenge can also be seen in the figures. The overdrive appears to be cutting the higher frequencies, behaving also as a low-pass filter.

For models trained on the Saturator dataset, the **LRU** model presents lower MSE and  $M_{RMSE}$  values, but when considering other metrics, no models appear clearly outperforming. When inspecting Figures 4, **LRU** is again left

Table 3: MSE test loss computed on the test set. The test sets include all conditioning values, if applicable. The last column reports the epoch at which the training met the early stopping condition.

Dataset	Model	MSE	Epoch	Dataset	Model	MSE	Epoch
OD300 Overdrive	LSTM	$2.46 \cdot 10^{-4}$	144	Neutron Overdrive	LSTM	$2.27 \cdot 10^{-3}$	4
	ED	$3.57 \cdot 10^{-4}$	176		ED	$2.79 \cdot 10^{-3}$	3
	LRU	$2.98 \cdot 10^{-4}$	170		LRU	$2.43 \cdot 10^{-3}$	100
	S4D	$3.23 \cdot 10^{-4}$	165		S4D	$2.62 \cdot 10^{-3}$	8
	S6	$3.39 \cdot 10^{-4}$	172		S6	$2.41 \cdot 10^{-3}$	28
Helper Saturator	LSTM	$4.56 \cdot 10^{-4}$	165	Pultec Passive Equalizer	LSTM	$7.41 \cdot 10^{-4}$	19
	ED	$4.41 \cdot 10^{-4}$	138		ED	$1.11 \cdot 10^{-3}$	101
	LRU	$4.14 \cdot 10^{-4}$	176		LRU	$1.03 \cdot 10^{-3}$	150
	S4D	$4.40 \cdot 10^{-4}$	149		S4D	$1.06 \cdot 10^{-3}$	11
	S6	$4.53 \cdot 10^{-4}$	188		S6	$9.68 \cdot 10^{-4}$	8
LA-2A Optical Compressor	LSTM	$1.11 \cdot 10^{-4}$	59	CL 1B Optical Compressor	LSTM	$1.78 \cdot 10^{-4}$	74
	ED	$9.54 \cdot 10^{-5}$	90		ED	$8.96 \cdot 10^{-5}$	38
	LRU	$1.14 \cdot 10^{-4}$	146		LRU	$6.76 \cdot 10^{-4}$	168
	S4D	$8.43 \cdot 10^{-5}$	62		S4D	$1.22 \cdot 10^{-4}$	14
	S6	$8.25 \cdot 10^{-5}$	42		S6	$1.01 \cdot 10^{-4}$	19
Neutron Filter	LSTM	$4.07 \cdot 10^{-3}$	46				
	ED	$3.36 \cdot 10^{-3}$	9				
	LRU	$2.43 \cdot 10^{-3}$	188				
	S4D	$2.75 \cdot 10^{-3}$	12				
	S6	$3.16 \cdot 10^{-3}$	7				

behind, while other models present closer performances. In contrast, **LRU** achieves closer matching in the spectrograms, visible in Figure 5. Other models tend to generate more harmonic, especially **LSTM** that introduces artifacts, which can be clearly heard when listening to the audio output and negatively affect its performance.

When training models with the Equalizer dataset, **LSTM** performs better in the time domain, having lower MSE and ESR errors while performing poorly in the frequency domain. Figures 4 show close performance among the models, while looking at the spectrograms **S6** present better matching. The optical compressor features a time-variant response with pronounced temporal dependencies, largely influenced by its variable attack and release parameters. This is especially noticeable in the case of the CL 1B compressor, which represents a more challenging task for neural network modeling. Among the tested models, the **LSTM** and **LRU** are the least accurate in the time domain metrics, exhibiting higher loss in both the LA-2A and CL 1B cases. In contrast, in the frequency domain, the gap is less prominent. The **S6** and **ED** models demonstrate superior accuracy for these two tasks. Specifically, **S6** outperforms the **ED** in the LA-2A case, while the **ED** excels in the CL 1B case. **S4D** presents similar performance than **S6**.

In the LA-2A case, we observe an overall good match for RMSE in Figure 4. The **LRU** model displays slightly more mismatches in both plots. Upon examining Figure 5, spectrograms related to the **S6** model have the best match with the target output, while the other models present similar mismatches when looking at the higher frequencies. More difficult is the CL 1B case, where **LRU** presents the best envelope matching in Figure 4, and Figure 5. In the case of the compressor, the capability to encode past information of the signal is critical, **LSTM** is confirmed to have a worse temporal tracking ability than the other models, which present design improvements. These improvements are particularly evident with the CL 1B when setting long attack and release time through the conditioning control parameters. These reach up to 300 ms and 5 seconds, respectively.

Modeling the low-pass filter is inherently a more complex task than the equalizer, given its more pronounced alterations to the frequency content of the processed signal. Nevertheless, informal listening evaluations of the predicted outputs indicate that all models struggle with accurately emulating the filter behavior; instead of eliminating high-frequency contents, they attenuate the whole signal, as apparent in Figure 5. However, when considering the quantitative metrics, the **LRU** model outperforms the others. The **LSTM** model, in particular, tends to incorrectly predict excessive energy on the RMS envelope, as visible in Figure 4, and to introduce artifact, as shown in Figure 5.

Table 4: ESR,  $M_{RMSE}$ ,  $M_{SF}$ , and  $M_{STFT}$  metrics computed on the test set. The test sets include all conditioning values, if applicable.

Dataset	Model	ESR	$M_{RMSE}$	$M_{SF}$	$M_{STFT}$	$M_{MFCC}$
OD300 Overdrive	LSTM	<b><math>1.06 \cdot 10^{-1}</math></b>	$1.06 \cdot 10^{-2}$	$1.60 \cdot 10^{-2}$	$3.56 \cdot 10^{-1}$	$6.08 \cdot 10^{-1}$
	ED	$1.54 \cdot 10^{-1}$	$1.30 \cdot 10^{-2}$	$1.19 \cdot 10^{-2}$	$3.52 \cdot 10^{-1}$	$5.80 \cdot 10^{-1}$
	LRU	$2.35 \cdot 10^{-1}$	$1.65 \cdot 10^{-2}$	$1.77 \cdot 10^{-2}$	$4.55 \cdot 10^{-1}$	1.05
	S4D	$1.40 \cdot 10^{-1}$	<b><math>1.20 \cdot 10^{-2}</math></b>	<b><math>8.50 \cdot 10^{-3}</math></b>	$3.11 \cdot 10^{-1}$	<b><math>5.38 \cdot 10^{-1}</math></b>
	S6	$1.46 \cdot 10^{-1}$	$1.25 \cdot 10^{-2}$	$1.04 \cdot 10^{-2}$	<b><math>2.78 \cdot 10^{-1}</math></b>	$5.61 \cdot 10^{-1}$
Neutron Overdrive	LSTM	<b><math>2.50 \cdot 10^{-1}</math></b>	<b><math>1.86 \cdot 10^{-2}</math></b>	$5.74 \cdot 10^{-3}$	$4.80 \cdot 10^{-1}$	$3.49 \cdot 10^{-1}$
	ED	$3.07 \cdot 10^{-1}$	$2.36 \cdot 10^{-2}$	$6.33 \cdot 10^{-3}$	$5.64 \cdot 10^{-1}$	$3.80 \cdot 10^{-1}$
	LRU	$2.70 \cdot 10^{-1}$	$1.94 \cdot 10^{-2}$	$6.64 \cdot 10^{-3}$	<b><math>3.40 \cdot 10^{-1}</math></b>	$3.39 \cdot 10^{-1}$
	S4D	$2.88 \cdot 10^{-1}$	$2.21 \cdot 10^{-2}$	$5.71 \cdot 10^{-3}$	$5.20 \cdot 10^{-1}$	$3.59 \cdot 10^{-1}$
	S6	$2.65 \cdot 10^{-1}$	$1.89 \cdot 10^{-2}$	<b><math>4.97 \cdot 10^{-3}</math></b>	$3.86 \cdot 10^{-1}$	<b><math>3.05 \cdot 10^{-1}</math></b>
Helper Saturator	LSTM	$2.67 \cdot 10^{-1}$	$1.05 \cdot 10^{-2}$	$2.78 \cdot 10^{-2}$	$5.97 \cdot 10^{-1}$	$4.72 \cdot 10^{-1}$
	ED	$2.58 \cdot 10^{-1}$	$1.06 \cdot 10^{-2}$	$1.29 \cdot 10^{-2}$	$5.33 \cdot 10^{-1}$	$4.14 \cdot 10^{-1}$
	LRU	$3.46 \cdot 10^{-1}$	<b><math>9.72 \cdot 10^{-3}</math></b>	$1.42 \cdot 10^{-2}$	$5.44 \cdot 10^{-1}$	<b><math>2.46 \cdot 10^{-1}</math></b>
	S4D	<b><math>2.57 \cdot 10^{-1}</math></b>	$1.06 \cdot 10^{-2}$	<b><math>1.22 \cdot 10^{-2}</math></b>	$5.41 \cdot 10^{-1}$	$3.67 \cdot 10^{-1}$
	S6	$2.65 \cdot 10^{-1}$	$1.01 \cdot 10^{-2}$	$1.31 \cdot 10^{-2}$	<b><math>4.28 \cdot 10^{-1}</math></b>	$3.88 \cdot 10^{-1}$
Pultec Passive Equalizer	LSTM	<b><math>2.15 \cdot 10^{-1}</math></b>	$1.29 \cdot 10^{-2}$	$8.85 \cdot 10^{-3}$	$9.33 \cdot 10^{-1}$	$2.06 \cdot 10^{-1}$
	ED	$3.22 \cdot 10^{-1}$	$1.24 \cdot 10^{-2}$	$2.49 \cdot 10^{-3}$	$4.94 \cdot 10^{-1}$	$1.91 \cdot 10^{-1}$
	LRU	$3.00 \cdot 10^{-1}$	<b><math>1.16 \cdot 10^{-2}</math></b>	$1.99 \cdot 10^{-3}$	<b><math>1.73 \cdot 10^{-1}</math></b>	$9.81 \cdot 10^{-2}$
	S4D	$3.08 \cdot 10^{-1}$	$1.19 \cdot 10^{-2}$	<b><math>1.79 \cdot 10^{-3}</math></b>	$4.09 \cdot 10^{-1}$	<b><math>9.44 \cdot 10^{-2}</math></b>
	S6	$2.80 \cdot 10^{-1}$	$1.19 \cdot 10^{-2}$	$3.89 \cdot 10^{-3}$	$2.87 \cdot 10^{-1}$	$1.26 \cdot 10^{-1}$
LA-2A Optical Compressor	LSTM	$1.03 \cdot 10^{-1}$	$4.51 \cdot 10^{-3}$	$1.12 \cdot 10^{-2}$	$4.37 \cdot 10^{-1}$	$3.10 \cdot 10^{-1}$
	ED	$8.91 \cdot 10^{-2}$	$4.10 \cdot 10^{-3}$	$7.28 \cdot 10^{-3}$	$2.30 \cdot 10^{-1}$	$2.30 \cdot 10^{-1}$
	LRU	$1.06 \cdot 10^{-1}$	$4.67 \cdot 10^{-3}$	$7.84 \cdot 10^{-3}$	$2.70 \cdot 10^{-1}$	$2.93 \cdot 10^{-1}$
	S4D	$7.87 \cdot 10^{-2}$	<b><math>3.51 \cdot 10^{-3}</math></b>	$1.00 \cdot 10^{-2}$	$2.52 \cdot 10^{-1}$	$2.53 \cdot 10^{-1}$
	S6	<b><math>7.71 \cdot 10^{-2}</math></b>	$3.63 \cdot 10^{-3}$	<b><math>6.26 \cdot 10^{-3}</math></b>	<b><math>1.84 \cdot 10^{-1}</math></b>	<b><math>2.12 \cdot 10^{-1}</math></b>
CL 1B Optical Compressor	LSTM	$2.92 \cdot 10^{-1}$	$9.33 \cdot 10^{-3}$	$5.21 \cdot 10^{-3}$	$3.56 \cdot 10^{-1}$	$2.26 \cdot 10^{-1}$
	ED	<b><math>1.46 \cdot 10^{-1}</math></b>	<b><math>4.05 \cdot 10^{-3}</math></b>	<b><math>4.18 \cdot 10^{-3}</math></b>	$4.17 \cdot 10^{-1}$	<b><math>2.09 \cdot 10^{-1}</math></b>
	LRU	$1.88 \cdot 10^{-2}$	$6.38 \cdot 10^{-3}$	$5.49 \cdot 10^{-3}$	$4.38 \cdot 10^{-1}$	$4.52 \cdot 10^{-1}$
	S4D	$2.00 \cdot 10^{-1}$	$5.02 \cdot 10^{-3}$	$6.12 \cdot 10^{-3}$	<b><math>2.79 \cdot 10^{-1}</math></b>	$2.93 \cdot 10^{-1}$
	S6	$1.67 \cdot 10^{-1}$	$4.41 \cdot 10^{-3}$	$6.23 \cdot 10^{-3}$	$4.99 \cdot 10^{-1}$	$2.36 \cdot 10^{-1}$
Neutron Filter	LSTM	1.06	$3.15 \cdot 10^{-2}$	$3.03 \cdot 10^{-2}$	$9.33 \cdot 10^{-1}$	$6.57 \cdot 10^{-1}$
	ED	$8.77 \cdot 10^{-1}$	$2.18 \cdot 10^{-2}$	$2.21 \cdot 10^{-2}$	$9.38 \cdot 10^{-1}$	$6.32 \cdot 10^{-1}$
	LRU	<b><math>6.58 \cdot 10^{-1}</math></b>	<b><math>1.66 \cdot 10^{-2}</math></b>	<b><math>1.95 \cdot 10^{-2}</math></b>	<b><math>7.51 \cdot 10^{-1}</math></b>	<b><math>5.98 \cdot 10^{-1}</math></b>
	S4D	$7.18 \cdot 10^{-1}$	$1.97 \cdot 10^{-2}$	$2.00 \cdot 10^{-2}$	$9.01 \cdot 10^{-1}$	$6.28 \cdot 10^{-1}$
	S6	$8.23 \cdot 10^{-1}$	$2.17 \cdot 10^{-2}$	$2.18 \cdot 10^{-2}$	$8.94 \cdot 10^{-1}$	$6.27 \cdot 10^{-1}$

Generally, performance metrics are relatively close across models across most effects examined in this study. Although the **S4D** model slightly outperforms other models based on the metrics alone, it appears to be the most suitable architecture analog effect modeling, at least considering those within the scope of this study. The **S6** model often performs very closely, while **LRU** presents the bigger variance across the different metrics and datasets.

The **ED** shows its quality when modeling the compressors. The **ED**, **LRU**, and particularly the **S4D** and **S6** models are more effective at encoding past signal information within their internal states. This is suggested by the case of the cases of optical compressors, where they significantly outperform other models. Conversely, the **LSTM** models appear to perform well only when emulating effects with shorter and less critical time dependencies, such as overdrive, equalizer, and filters. Moreover, **LSTM** models tend to introduce artifacts in some cases.

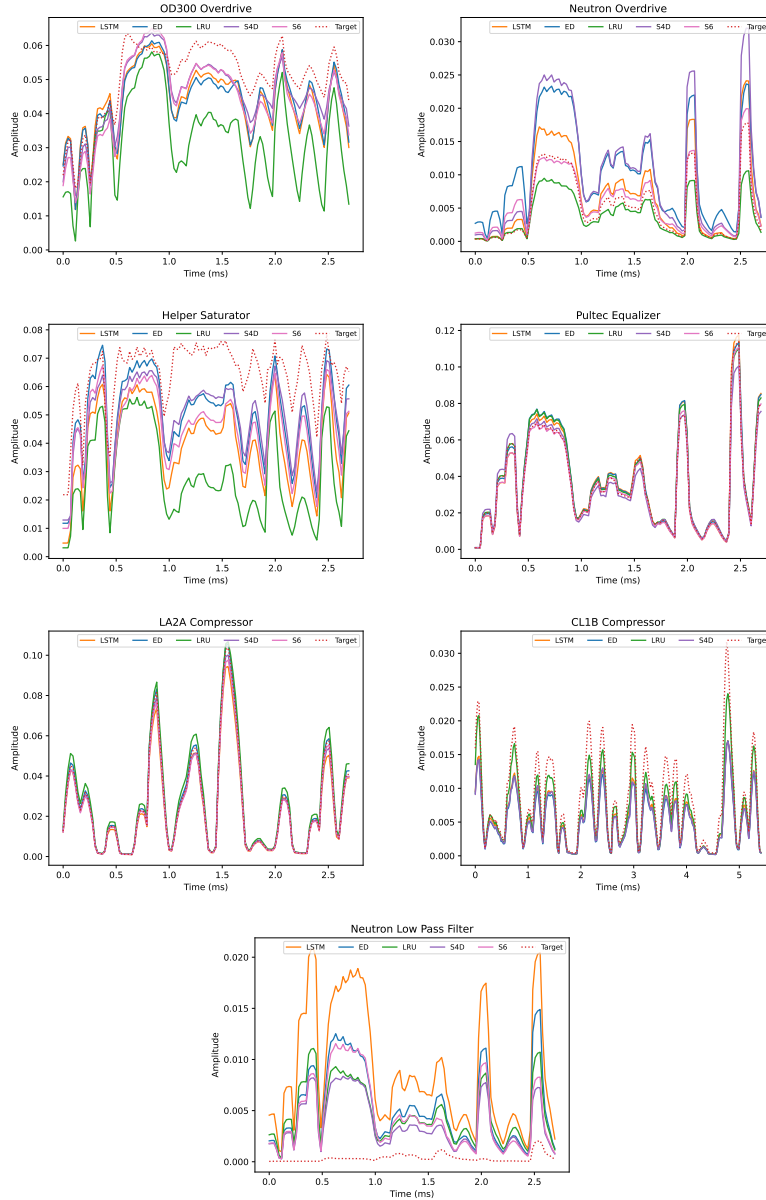


Figure 4: Comparison of the RMSE between the target and predicted output. The RMSE is computed using windows of 4096 samples with 75% overlap. When the model includes conditioning, the results refer to the highest conditioning values, representing the most challenging scenario.

## 5 Conclusion

The computational challenges of simulating the nonlinearities of analog effect, described by complex differential equations, are a significant obstacle for real-time applications. The complexity of these nonlinearities makes them difficult to model accurately, but they also contribute to the unique sound characteristics of the devices, making them appealing for both academic and industrial purposes. Modeling these nonlinear aspects is a difficult task that requires simplifications and assumptions to ensure stability and efficiency in the numerical schemes. Artificial neural networks (ANN) have emerged as a popular data-driven approach for this modeling process. While they offer a convenient and automated approach, they may struggle with the computational complexity and flexibility required for handling control parameters. In some cases, hybrid solutions that incorporate physics knowledge or measurements from internal components may provide advantages. However, there are situations where black-box models are necessary and feasible.

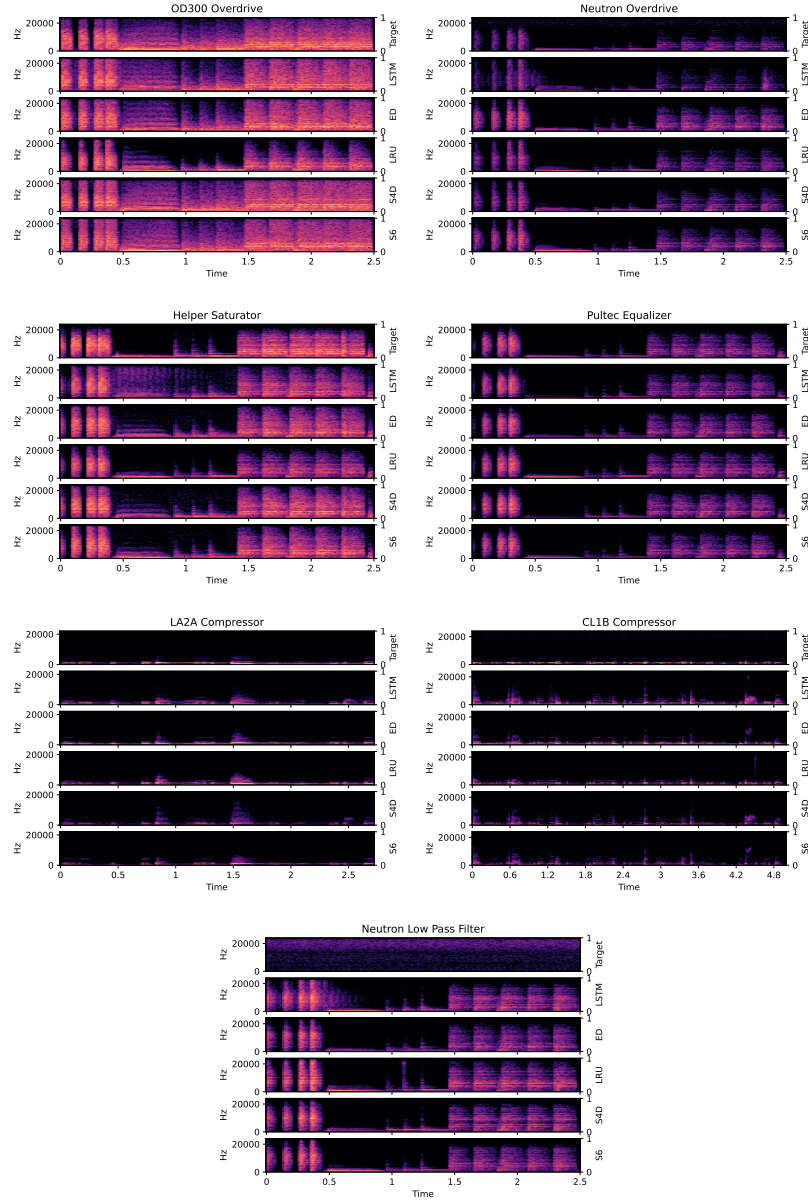


Figure 5: Comparison of spectrograms of the target and predicted output. The STFT is computed using windows of 2048 samples with 25% overlap. The results refer to the highest conditioning values, representing the most challenging scenario.

Recurrent neural networks (RNNs) utilize internal states as memory mechanisms, allowing them to encode the signal history. This feature enables more interactive solutions as their memory capacity is not solely dependent on the input amount. In this paper, we present a comparative analysis that examines the performance of the widely used Long Short-Term Memory (LSTM) models against recently proposed recurrent models, namely Linear Recurrent Unit (LRU) and State-Space models (SSM), which have demonstrated remarkable results in sequence modeling. To carry out this study, we design five models incorporating parameter conditioning and providing low-latency response. The control parameters are integrated into the models using the Feature-wise Linear Modulation (FiLM) method. Our selection of effects includes overdrive, saturation, low pass filter, equalization, and compressors. We evaluate these models using various metrics, which provide valuable insights for future research and development. Specifically, our metrics consider the root-mean-squared energy envelopes, the transients, and the frequency content.



LSTM-based networks excel in replicating distortion and equalizer effects, showing their ability to encode the audio dependencies enough for these specific effects effectively. Conversely, LSTMs tend to introduce more artifacts than other models considered in this study. In contrast, LSTM, when designed in an encoder-decoder fashion, LRUs and, in particular, SSMs, outperform other models when emulating saturation and compression. In the case of compression, they demonstrate their advantage in accurately capturing the signal’s history. Generally, SSMs have also proved to be an appropriate candidate technique in VA, although the gap with the other models is not always so pronounced. Lastly, LRUs are less consistent in their quality across the different metrics.

In this study, we did not carry out architecture—and effect-specific optimizations, which can definitely boost the accuracy, such as tuning hyperparameters and changing the size of the various layers. We limited computational complexity and input-output latency and focused the study on models that can be theoretically implemented in consumer-grade devices for live audio applications.

## References

- Chowdhury, J. 2020. A comparison of virtual analog modelling techniques for desktop and embedded implementations. *arXiv preprint arXiv:2009.02833*.
- Chowdhury, J, & Clarke, CJ. 2022. Emulating Diode Circuits with Differentiable Wave Digital Filters.
- Covert, J, & Livingston, DL. 2013. A vacuum-tube guitar amplifier model using a recurrent neural network. *Pages 1–5 of: 2013 Proceedings of IEEE Southeastcon*. IEEE.
- Damskäg, E-P, Juvela, L, Thuillier, E, & Välimäki, V. 2019a. Deep learning for tube amplifier emulation. *Pages 471–475 of: ICASSP 2019-2019 IEEE International Conference on Acoustics, Speech and Signal Processing (ICASSP)*. IEEE.
- Damskäg, E-P, Juvela, L, & Välimäki, V. 2019b. Real-time modeling of audio distortion circuits with deep learning. *Pages 332–339 of: Proc. Int. Sound and Music Computing Conf.(SMC-19), Malaga, Spain*.
- Darabundit, C, Wedelich, R, Little, F, NJ, P, & Bischoff, P. 2019. DIGITAL GREY BOX MODEL OF THE UNI-VIBE EFFECTS PEDAL.
- Darabundit, C, Roosenburg, D, & III, JO Smith. 2022. Neural net tube models for wave digital filters. *Pages 153–160 of: Proc. 25th Int. Conf. Digital Audio Effects (DAFx20in22)*. Vienna University of Music and Performing Arts Vienna.
- Dauphin, YN, Fan, A, Auli, M, & Grangier, D. 2017. Language modeling with gated convolutional networks. *Pages 933–941 of: International conference on machine learning*. PMLR.
- Eichas, F, & Zölzer, U. 2016. Black-box modeling of distortion circuits with block-oriented models. *Pages 5–9 of: Proceedings of the International Conference on Digital Audio Effects (DAFx), Brno, Czech Republic*.
- Eichas, F, Möller, S, & Zölzer, U. 2015. Block-oriented modeling of distortion audio effects using iterative minimization. *Proc. Digital Audio Effects (DAFx-15), Trondheim, Norway*.
- Eichas, F, Möller, S, & Zölzer, U. 2017. Block-oriented gray box modeling of guitar amplifiers. *Pages 5–9 of: Proceedings of the International Conference on Digital Audio Effects (DAFx), Edinburgh, UK*.
- Engel, Jesse, Hantrakul, Lamtharn (Hanoi), Gu, Chenjie, & Roberts, Adam. 2020. DDSP: Differentiable Digital Signal Processing. *In: International Conference on Learning Representations*.
- Esqueda, F, Kuznetsov, B, & Parker, JD. 2021. DIFFERENTIABLE WHITE-BOX VIRTUAL ANALOG MODELING.
- Fasciani, S., Simionato, R., & Tidemann, A. 2024a. Conditioning Methods for Neural Audio Effects.
- Fasciani, S., Simionato, R., & Tidemann, A. 2024b. A Universal TOOL FOR GENERATING DATASETS FROM AUDIO EFFECTS.
- Gu, A., & Dao, T. 2023. Mamba: Linear-time sequence modeling with selective state spaces. *arXiv preprint arXiv:2312.00752*.
- Gu, A, Albert, Dao, T, Ermon, S, Stefano, Rudra, A, & Ré, C. 2020. Hippo: Recurrent memory with optimal polynomial projections. *Advances in neural information processing systems*, **33**, 1474–1487.
- Gu, A, Goel, K, Gupta, A, & Ré, C. 2022a. On the parameterization and initialization of diagonal state space models. *Advances in Neural Information Processing Systems*, **35**, 35971–35983.
- Gu, Albert, Goel, Karan, & Ré, Christopher. 2022b. Efficiently Modeling Long Sequences with Structured State Spaces. *In: The International Conference on Learning Representations (ICLR)*.
- Hochreiter, S, & Schmidhuber, J. 1997. Long short-term memory. *Neural computation*, **9**(8), 1735–1780.

- Hou, L, Samaras, D, Kurc, T, Gao, Y, & Saltz, J. 2017. Convnets with smooth adaptive activation functions for regression. *Pages 430–439 of: Artificial Intelligence and Statistics*. PMLR.
- Jr, A Schuck, & Bodmann, BEJ. 2016. Audio nonlinear modeling through hyperbolic tangent functionals. *Pages DAFX103–DAFX108 of: Proceedings of the 19th International Conference on Digital Audio Effects (DAFx-16)*.
- Kingma, DP, & Ba, J. 2014. Adam: A method for stochastic optimization. *Int. Conf. on Learning Representations*.
- Köper, L, & Holters, M. 2020. TAMING THE RED LLAMA—MODELING A CMOS-BASED OVERDRIVE CIRCUIT.
- Kuznetsov, B, Parker, JD, & Esqueda, F. 2020. Differentiable IIR filters for machine learning applications. *Pages 297–303 of: Proc. Int. Conf. Digital Audio Effects (eDAFx-20)*.
- LeCun, Y, Bottou, L, Bengio, Y, & Haffner, P. 1998. Gradient-based learning applied to document recognition. *Proceedings of the IEEE*, **86**(11), 2278–2324.
- Mendoza, DS. 2005. *Emulating electric guitar effects with neural networks*. Barcelona, Spain: Universitat Pompeu Fabra.
- Mikkonen, O, Wright, A, Moliner, E, & Välimäki, V. 2023. Neural modeling of magnetic tape recorders. *In: Proceedings of the International Conference on Digital Audio Effects*.
- Miklanek, S, Wright, A, Välimäki, V, & Schimmel, J. 2023. Neural Grey-Box Guitar Amplifier Modelling With Limited Data. *Pages 151–158 of: International Conference on Digital Audio Effects*. Aalborg University.
- Nercessian, S, Sarroff, A, & Werner, KJ. 2021. Lightweight and interpretable neural modeling of an audio distortion effect using hyperconditioned differentiable biquads. *Pages 890–894 of: ICASSP 2021-2021 IEEE International Conference on Acoustics, Speech and Signal Processing (ICASSP)*. IEEE.
- Oord, A, Dieleman, S, Zen, H, Heiga, Simonyan, K, Vinyals, O, Graves, A, Kalchbrenner, N, Senior, A, & Kavukcuoglu, K. 2016. Wavenet: A generative model for raw audio. *arXiv preprint arXiv:1609.03499*.
- Orvieto, Antonio, Smith, Samuel L, Gu, Albert, Fernando, Anushan, Gulcehre, Caglar, Pascanu, Razvan, & De, Soham. 2023. Resurrecting recurrent neural networks for long sequences. *Pages 26670–26698 of: International Conference on Machine Learning*. PMLR.
- Parker, JD, Esqueda, F, & Bergner, A. 2019. Modelling of nonlinear state-space systems using a deep neural network. *Pages 2–6 of: Proceedings of the 23rd International Conference on Digital Audio Effects (DAFx-19), Birmingham, UK*.
- Pascanu, R, Mikolov, T, & Bengio, Y. 2013. On the difficulty of training recurrent neural networks. *Pages 1310–1318 of: International conference on machine learning*. Pmlr.
- Perez, E, Strub, F, Vries, H De, Dumoulin, V, & Courville, A. 2018. Film: Visual reasoning with a general conditioning layer. *In: Proceedings of the AAAI conference on artificial intelligence*, vol. 32.
- Primavera, A, Gasparini, M, Cecchi, S, Hariya, W, Murai, S, Oishi, K, Piazza, F, & Francesco. 2018. A novel measurement procedure for Wiener/Hammerstein classification of nonlinear audio systems. *In: Audio Engineering Society Convention 144*. Audio Engineering Society.
- Ramírez, MAM, JD, & Reiss. 2019. Modeling nonlinear audio effects with end-to-end deep neural networks. *Pages 171–175 of: ICASSP 2019-2019 IEEE International Conference on Acoustics, Speech and Signal Processing (ICASSP)*. IEEE.
- Ramírez, MAM, Benetos, E, & Reiss, JD. 2020a. Deep learning for black-box modeling of audio effects. *Applied Sciences*, **10**(2), 638.
- Ramírez, MAM, Benetos, E, Emmanouil, & Reiss, JD. 2020b. Modeling plate and spring reverberation using a dsp-informed deep neural network. *Pages 241–245 of: ICASSP 2020-2020 IEEE International Conference on Acoustics, Speech and Signal Processing (ICASSP)*. IEEE.
- Schoukens, M, & Tiels, K. 2017. Identification of block-oriented nonlinear systems starting from linear approximations: A survey. *Automatica*, **85**, 272–292.
- Simionato, R, & Fasciani, S. 2022. Deep Learning Conditioned Modeling of Optical Compression. DAFx Board.
- Simionato, R, & Fasciani, S. 2023. Fully Conditioned and Low-latency Black-box Modeling of Analog Compression. DAFx Board.
- Steinmetz, J., Christian, Reiss, & D., Joshua. 2022. Efficient neural networks for real-time analog audio effect modeling.
- Wilczek, J, Wright, A, Välimäki, V, & Habets, E. 2022. Virtual Analog Modeling of Distortion Circuits Using Neural Ordinary Differential Equations. *Proc. Int. Conf. Digital Audio Effects (DAFx-22), Vienna, Austria*.

- Wright, A., & Välimäki, V. 2021. Neural modeling of phaser and flanging effects. *Journal of the Audio Engineering Society*, **69**(7/8), 517–529.
- Wright, A., & Välimäki, V. 2022. Grey-box modelling of dynamic range compression. *Proc. Int. Conf. Digital Audio Effects (DAFx-22)*, Vienna, Austria.
- Wright, A., Damskögg, Alec E-P, Välimäki, V., & Vesa. 2019. Real-time black-box modelling with recurrent neural networks. *In: 22nd international conference on digital audio effects (DAFx-19)*.